

# Graphene photonics and optoelectronics

F. Bonaccorso, Z. Sun, T. Hasan and A. C. Ferrari\*

**The richness of optical and electronic properties of graphene attracts enormous interest. Graphene has high mobility and optical transparency, in addition to flexibility, robustness and environmental stability. So far, the main focus has been on fundamental physics and electronic devices. However, we believe its true potential lies in photonics and optoelectronics, where the combination of its unique optical and electronic properties can be fully exploited, even in the absence of a bandgap, and the linear dispersion of the Dirac electrons enables ultrawideband tunability. The rise of graphene in photonics and optoelectronics is shown by several recent results, ranging from solar cells and light-emitting devices to touch screens, photodetectors and ultrafast lasers. Here we review the state-of-the-art in this emerging field.**

Electrons propagating through the bidimensional structure of graphene have a linear relation between energy and momentum, and thus behave as massless Dirac fermions<sup>1–3</sup>. Consequently, graphene exhibits electronic properties for a two-dimensional (2D) gas of charged particles described by the relativistic Dirac equation, rather than the non-relativistic Schrödinger equation with an effective mass<sup>1,2</sup>, with carriers mimicking particles with zero mass and an effective ‘speed of light’ of around  $10^6$  m s<sup>−1</sup>.

Graphene exhibits a variety of transport phenomena that are characteristic of 2D Dirac fermions, such as specific integer and fractional quantum Hall effects<sup>4,5</sup>, a ‘minimum’ conductivity of  $\sim 4e^2/h$  even when the carrier concentration tends to zero<sup>1</sup>, and Shubnikov–de Haas oscillations with a  $\pi$  phase shift due to Berry’s phase<sup>1</sup>. Mobilities ( $\mu$ ) of up to  $10^6$  cm<sup>2</sup> V<sup>−1</sup> s<sup>−1</sup> are observed in suspended samples. This, combined with near-ballistic transport at room temperature, makes graphene a potential material for nano-electronics<sup>6,7</sup>, particularly for high-frequency applications<sup>8</sup>.

Graphene also shows remarkable optical properties. For example, it can be optically visualized, despite being only a single atom thick<sup>9,10</sup>. Its transmittance ( $T$ ) can be expressed in terms of the fine-structure constant<sup>11</sup>. The linear dispersion of the Dirac electrons makes broadband applications possible. Saturable absorption is observed as a consequence of Pauli blocking<sup>12,13</sup>, and non-equilibrium carriers result in hot luminescence<sup>14–17</sup>. Chemical and physical treatments can also lead to luminescence<sup>18–21</sup>. These properties make it an ideal photonic and optoelectronic material.

## Electronic and optical properties

**Electronic properties.** The electronic structure of single-layer graphene (SLG) can be described using a tight-binding Hamiltonian<sup>2,3</sup>. Because the bonding and anti-bonding  $\sigma$ -bands are well separated in energy ( $>10$  eV at the Brillouin zone centre  $\Gamma$ ), they can be neglected in semi-empirical calculations, retaining only the two remaining  $\pi$ -bands<sup>3</sup>. The electronic wavefunctions from different atoms on the hexagonal lattice overlap. However, any such overlap between the  $p_z(\pi)$  and the  $s$  or  $p_x$  and  $p_y$  orbitals is strictly zero by symmetry. Consequently, the  $p_z$  electrons, which form the  $\pi$ -bonds, can be treated independently from the other valence electrons. Within this  $\pi$ -band approximation it is easy to describe the electronic spectrum of the total Hamiltonian and to obtain the dispersion relations  $E^\pm(k_x, k_y)$  restricted to first-nearest-neighbour interactions only:

$$E^\pm(k_x, k_y) = \pm \gamma_0 \sqrt{1 + 4 \cos \frac{\sqrt{3} k_x a}{2} \cos \frac{k_y a}{2} + 4 \cos^2 \frac{k_y a}{2}} \quad (1)$$

where  $a = \sqrt{3} a_{cc}$  (with  $a_{cc} = 1.42$  Å being the carbon–carbon distance) and  $\gamma_0$  is the transfer integral between first-neighbour  $\pi$ -orbitals (typical values for  $\gamma_0$  are 2.9–3.1 eV). The  $\mathbf{k} = (k_x, k_y)$  vectors in the first Brillouin zone constitute the ensemble of available electronic momenta.

With one  $p_z$  electron per atom in the  $\pi$ - $\pi^*$  model (the three other  $s, p_x, p_y$  electrons fill the low-lying  $\sigma$ -band), the (−) band (negative energy branch) in equation (1) is fully occupied, whereas the (+) branch is totally empty. These occupied and unoccupied bands touch at the  $\mathbf{K}$  points. The Fermi level  $E_F$  is the zero-energy reference, and the Fermi surface is defined by  $\mathbf{K}$  and  $\mathbf{K}'$ . Expanding equation (1) at  $\mathbf{K}(\mathbf{K}')$  yields the linear  $\pi$ - and  $\pi^*$ -bands for Dirac fermions:

$$E^\pm(\mathbf{\kappa}) = \pm \hbar v_F |\mathbf{\kappa}| \quad (2)$$

where  $\mathbf{\kappa} = \mathbf{k} - \mathbf{K}$  and  $v_F$  is the electronic group velocity, which is given by  $v_F = \sqrt{3} \gamma_0 a / (2\hbar) \approx 10^6$  m s<sup>−1</sup>.

The linear dispersion given by equation (2) is the solution to the following effective Hamiltonian at the  $\mathbf{K}(\mathbf{K}')$  point  $\mathbf{H} = \pm \hbar v_F (\boldsymbol{\sigma} \cdot \mathbf{\kappa})$ , where  $\mathbf{\kappa} = -i\nabla$  and  $\boldsymbol{\sigma}$  are the pseudo-spin Pauli matrices operating in the space of the electron amplitude on the A–B sublattices of graphene<sup>2,3</sup>.

**Linear optical absorption.** The optical image contrast can be used to identify graphene on top of a Si/SiO<sub>2</sub> substrate (Fig. 1a)<sup>9</sup>. This scales with the number of layers and is the result of interference, with SiO<sub>2</sub> acting as a spacer. The contrast can be maximized by adjusting the spacer thickness or the light wavelength<sup>9,10</sup>. The transmittance of a freestanding SLG can be derived by applying the Fresnel equations in the thin-film limit for a material with a fixed universal optical conductance<sup>22</sup>  $G_0 = e^2/(4\hbar) \approx 6.08 \times 10^{-5} \Omega^{-1}$ , to give:

$$T = (1 + 0.5\pi\alpha)^{-2} \approx 1 - \pi\alpha \approx 97.7\% \quad (3)$$

where  $\alpha = e^2/(4\pi\epsilon_0\hbar c) = G_0/(\pi\epsilon_0 c) \approx 1/137$  is the fine-structure constant<sup>11</sup>. Graphene only reflects  $<0.1\%$  of the incident light in the visible region<sup>11</sup>, rising to  $\sim 2\%$  for ten layers<sup>9</sup>. Thus, we can take

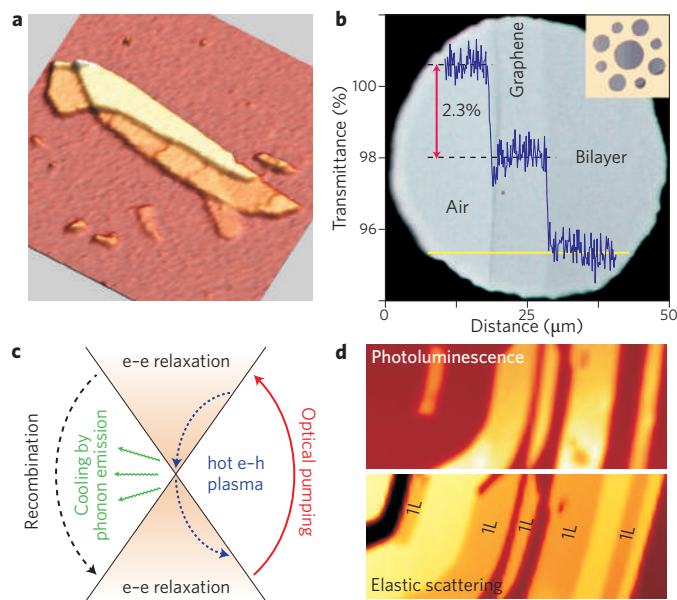


**Figure 1 | The optical properties of graphene.** **a**, Elastic light scattering (Rayleigh) image of a graphite flake with varying number of graphene layers<sup>9</sup>. **b**, Transmittance for an increasing number of layers. Inset, sample design for the experiment of ref. 11, showing a thick metal support structure with several apertures, on top of which graphene flakes are placed. **c**, Schematic of photoexcited electron kinetics in graphene, with possible relaxation mechanisms for the non-equilibrium electron population. **d**, Photoluminescence (top) and elastic scattering (bottom) images of an oxygen-treated flake<sup>18</sup>. 1L indicates single-layer graphene. Figure reproduced with permission from: **a**, ref. 9, © 2007 ACS; **b**, ref. 11, © 2008 AAAS; **c**, ref. 13, © 2010 ACS; **d**, ref. 18, © 2009 ACS.

the optical absorption of graphene layers to be proportional to the number of layers, each absorbing  $A \approx 1 - T \approx \pi\alpha \approx 2.3\%$  over the visible spectrum (Fig. 1b). In a few-layer graphene (FLG) sample, each sheet can be seen as a 2D electron gas, with little perturbation from the adjacent layers, making it optically equivalent to a superposition of almost non-interacting SLG<sup>9</sup>. The absorption spectrum of SLG is quite flat from 300 to 2,500 nm with a peak in the ultraviolet region ( $\sim 270$  nm), due to the exciton-shifted van Hove singularity in the graphene density of states. In FLG, other absorption features can be seen at lower energies, associated with interband transitions<sup>23,24</sup>.

**Saturable absorption.** Interband excitation by ultrafast optical pulses produces a non-equilibrium carrier population in the valence and conduction bands (Fig. 1c). In time-resolved experiments<sup>25</sup>, two relaxation timescales are typically seen: a faster one of  $\sim 100$  fs that is usually associated with carrier-carrier intraband collisions and phonon emission, and a slower one, on a picosecond timescale, which corresponds to electron interband relaxation and cooling of hot phonons<sup>26,27</sup>.

The linear dispersion of the Dirac electrons implies that for any excitation there will always be an electron-hole pair in resonance. A quantitative treatment of the electron-hole dynamics requires the solution of the kinetic equation for the electron and hole distribution functions,  $f_e(\mathbf{p})$  and  $f_h(\mathbf{p})$ ,  $\mathbf{p}$  being the momentum counted from the Dirac point<sup>13</sup>. If the relaxation times are shorter than the pulse duration, then during the pulse the electrons reach a stationary state, and collisions put electrons and holes into thermal equilibrium at an effective temperature<sup>13</sup>. The populations determine electron and hole densities, total energy density and a reduction of photon absorption per layer, due to Pauli blocking, by a factor of

$\Delta A/A = [1 - f_e(\mathbf{p})][1 - f_h(\mathbf{p})] - 1$ . Assuming efficient carrier-carrier relaxation (both intraband and interband) and efficient cooling of the graphene phonons, the main bottleneck is energy transfer from electrons to phonons<sup>13</sup>.

For linear dispersions near the Dirac point, pair-carrier collisions cannot lead to interband relaxation, thereby conserving the total number of electrons and holes separately<sup>13,28</sup>. Interband relaxation by phonon emission can occur only if the electron and hole energies are close to the Dirac point (within the phonon energy). Radiative recombination of the hot electron-hole population has also been suggested<sup>14-17</sup>. For graphite flakes, the dispersion is quadratic and pair-carrier collisions can lead to interband relaxation. Thus, in principle, decoupled SLG can provide the highest saturable absorption for a given amount of material<sup>13</sup>.

**Luminescence.** Graphene could be made luminescent by inducing a bandgap, following two main routes. One is by cutting it into ribbons and quantum dots, the other is by chemical or physical treatments, to reduce the connectivity of the  $\pi$ -electron network. Even though graphene nanoribbons have been produced with varying bandgaps<sup>7</sup>, as yet no photoluminescence has been reported from them. However, bulk graphene oxide dispersions and solids do show a broad photoluminescence<sup>19-21,29</sup>. Individual graphene flakes can be made brightly luminescent by mild oxygen plasma treatment<sup>18</sup>. The resulting photoluminescence is uniform across large areas, as shown in Fig. 1d, in which a photoluminescence map and the corresponding elastic scattering image are compared. It is possible to make hybrid structures by etching just the top layer, while leaving underlying layers intact<sup>18</sup>. This combination of photoluminescent and conductive layers could be used in sandwich light-emitting diodes. Luminescent graphene-based materials can now be routinely produced that cover the infrared, visible and blue spectral ranges<sup>18-21,29</sup>.

Even though some groups have ascribed photoluminescence in graphene oxide to bandgap emission from electron-confined  $sp^2$  islands<sup>19-21</sup>, this is more likely to arise from oxygen-related defect states<sup>18</sup>. Whatever the origin, fluorescent organic compounds are of importance to the development of low-cost optoelectronic devices<sup>30</sup>. Blue photoluminescence from aromatic or olefinic molecules is particularly important for display and lighting applications<sup>31</sup>. Luminescent quantum dots are widely used for bio-labelling and bio-imaging. However, their toxicity and potential environmental hazard limit widespread use and *in vivo* applications. Fluorescent bio-compatible carbon-based nanomaterials may be a more suitable alternative. Fluorescent species in the infrared and near-infrared are useful for biological applications, because cells and tissues show little auto-fluorescence in this region<sup>32</sup>. Sun *et al.* exploited photoluminescent graphene oxide for live cell imaging in the near-infrared with little background<sup>20</sup>.

Wang *et al.* have reported a gate-controlled, tunable gap up to 250 meV in bilayer graphene<sup>23</sup>. This may make new photonic devices possible for far-infrared light generation, amplification and detection.

Broadband nonlinear photoluminescence is also possible following non-equilibrium excitation of untreated graphene layers (Fig. 1c), as recently reported by several groups<sup>14-17</sup>. Emission occurs throughout the visible spectrum, for energies both higher and lower than the exciting one, in contrast with conventional photoluminescence processes<sup>14-17</sup>. This broadband nonlinear photoluminescence is thought to result from radiative recombination of a distribution of hot electrons and holes, generated by rapid scattering between photoexcited carriers after the optical excitation<sup>14-17</sup>, their temperature being determined by interactions with strongly coupled optical phonons<sup>15</sup>. It scales with the number of layers and can be used as a quantitative imaging tool, as well as to reveal the dynamics of the hot electron-hole plasma<sup>14-17</sup> (Fig. 1c). As for oxygen-induced luminescence, further work is necessary to fully explain this hot luminescence.

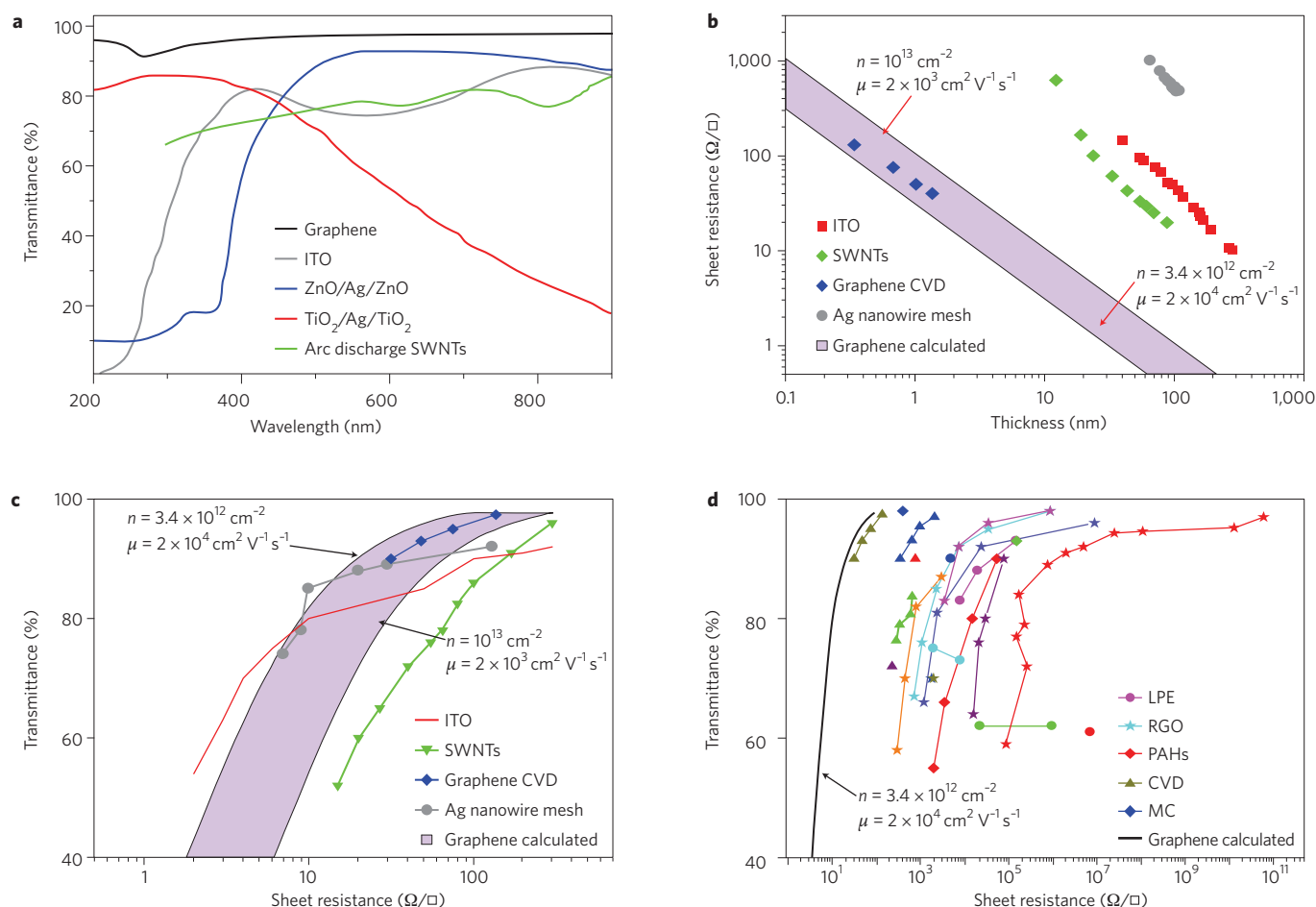


**Figure 2 | Graphene as transparent conductor.** **a**, Transmittance for different transparent conductors: GTCFs<sup>39</sup>, single-walled carbon nanotubes (SWNTs)<sup>77</sup>, ITO<sup>75</sup>, ZnO/Ag/ZnO (ref. 81) and TiO<sub>2</sub>/Ag/TiO<sub>2</sub> (ref. 70). **b**, Thickness dependence of the sheet resistance. The blue rhombuses show roll-to-roll GTCFs based on CVD-grown graphene<sup>39</sup>; red squares, ITO<sup>75</sup>; grey dots, metal nanowires<sup>75</sup>; green rhombuses, SWNTs<sup>77</sup>. Two limiting lines for GTCFs are also plotted (enclosing the shaded area), calculated from equation (6) using typical values for  $n$  and  $\mu$ . **c**, Transmittance versus sheet resistance for different transparent conductors: blue rhombuses, roll-to-roll GTCFs based on CVD-grown graphene<sup>39</sup>; red line, ITO<sup>75</sup>; grey dots, metal nanowires<sup>75</sup>; green triangles, SWNTs<sup>77</sup>. Shaded area enclosed by limiting lines for GTCFs calculated using  $n$  and  $\mu$  as in **b**. **d**, Transmittance versus sheet resistance for GTCFs grouped according to production strategies: triangles, CVD<sup>37–39,97</sup>; blue rhombuses, micromechanical cleavage (MC)<sup>88</sup>; red rhombuses, organic synthesis from polyaromatic hydrocarbons (PAHs)<sup>65</sup>; dots, liquid-phase exfoliation (LPE) of pristine graphene<sup>44,45,48,88</sup>; and stars, reduced graphene oxide (RGO)<sup>52,54,83,84,96</sup>. A theoretical line as for equation (6) is also plotted for comparison.

Electroluminescence was also recently reported in pristine graphene<sup>33</sup>. Although the power conversion efficiency is lower than it is for carbon nanotubes (CNTs), this could lead to new light-emitting devices based entirely on graphene.

## Production

Graphene was first produced by micromechanical exfoliation of graphite<sup>34</sup>. This approach still gives the best samples in terms of purity, defects, mobility and optoelectronic properties. However, it is clear that large-scale assembly is needed for the widespread application of this material. Several approaches have been developed to provide a steady supply of graphene in large areas and quantities, amenable for mass applications. These include growth by chemical vapour deposition (CVD)<sup>35–39</sup>, segregation by heat treatment of carbon-containing substrates<sup>40–42</sup>, and liquid phase exfoliation<sup>43–47</sup>. In fact, most of these methods date back several decades. The current interest in graphene has pushed these early approaches to large yields, controlled growth and large areas, and made it possible in just six years to go from micrometre-sized flakes to near-mass-production of layer-controlled samples.

**Micromechanical cleavage.** This method involves peeling off a piece of graphite by means of adhesive tape<sup>34</sup>. It has been optimized to produce SLG of up to millimetres in size, and with high structural and electronic quality. Although this is the method of choice for fundamental research, with most key results on individual SLG being obtained on such flakes, it has disadvantages in terms of yield and throughput, and is impractical for large-scale applications.

**Liquid-phase exfoliation.** Liquid-phase exfoliation (LPE) consists of chemical wet dispersion followed by ultrasonication, in both aqueous<sup>45</sup> and non-aqueous solvents<sup>44</sup>. Up to ~70% SLG can be achieved by mild sonication in water with sodium deoxycholate followed by sedimentation-based ultracentrifugation. Bile salt surfactants also allow the isolation of flakes with controlled thickness, when combined with density gradient ultracentrifugation<sup>48</sup>. Exfoliation of graphite-intercalated compounds<sup>46</sup> and expandable graphite<sup>49</sup> has also been reported.

LPE can also produce graphene nanoribbons with widths less than 10 nm (ref. 43) and offers advantages of scalability and no requirement for expensive growth substrates. Furthermore, it is an ideal means to produce films and composites.

**Graphene oxide.** Sonication of graphite oxide can be used to produce graphene oxide<sup>47</sup>, following the 50-year-old Hummers method<sup>50</sup>. The oxidation of graphite in the presence of acids and oxidants, proposed in the nineteenth century<sup>51</sup>, disrupts the  $sp^2$  network and introduces hydroxyl or epoxide groups<sup>52,53</sup> with carboxylic or carbonyl groups attached to the edges. These make graphene oxide sheets readily dispersible in water and several other solvents. Although large flakes can be obtained, these are intrinsically defective and electrically insulating. Despite several attempts<sup>47,52</sup>, reduced graphene oxide does not fully regain the pristine graphene electrical conductivity<sup>52,54</sup>. It is therefore important to distinguish between dispersion-processed graphene flakes, which retain the electronic properties of graphene, and insulating graphene oxide layers.

**Chemical vapour deposition.** The CVD of FLGs was reported more than 40 years ago<sup>35</sup>. SLG and FLG can now be grown on various substrates by feeding hydrocarbons at a suitable temperature<sup>35–39,55,56</sup>. The scale of progress in CVD growth is given by ref. 39, in which samples of over 60 cm were reported. Plasma-enhanced CVD can be applied on substrates without a catalyst<sup>56</sup>. Note that most as-grown CVD samples are multilayered. Even if their Raman spectrum seems similar<sup>37,38</sup> to that of ideal SLG<sup>57</sup>, this is just an indication of electronic decoupling of the layers, not definite proof of SLG growth.

**Carbon segregation.** Graphene can also be produced through carbon segregation from silicon carbide<sup>40,58,59</sup> (SiC) or metal substrates<sup>41,55,60–62</sup> following high-temperature annealing. Acheson reported<sup>58</sup> a method of producing graphite from SiC in as early as 1896, and the segregation of graphene from Ni(111) was investigated over 30 years ago<sup>60</sup>. High-quality layers can now be produced on SiC in an argon atmosphere<sup>42</sup>, and electronic decoupling from the underlying SiC substrate can be achieved by hydrogen treatment<sup>63</sup>.

**Chemical synthesis.** Graphene or carbon nanosheets can be produced through chemical synthesis<sup>64</sup>. Total organic synthesis yields graphene-like polyaromatic hydrocarbons<sup>65</sup>. These synthetic nanographenes can then be assembled to form larger layers, or to achieve atomically precise bottom-up fabrication of nanoribbons. Supramolecular interactions can be used to cover SLG with polyaromatic hydrocarbons, keeping the  $sp^2$  network intact without compromising the transport properties. Nanographenes form ordered layers, with precise control of orientation and spacing<sup>66</sup>. These interact with the graphene backbone, making it possible, in principle, to control and tune its optoelectronic properties<sup>66</sup>.

**Deterministic placement.** A fundamental step in the production of useful devices is the deterministic placement of graphene on pre-defined positions on a substrate of choice. Transfer processes are common in the semiconductor industry, and extensive experience of transfer has been developed for CNTs. Reina *et al.* reported transfer of SLG and FLG from  $\text{SiO}_2/\text{Si}$  to other substrates<sup>67</sup>. A layer of poly(methyl methacrylate) (PMMA) was coated on graphene deposited on  $\text{SiO}_2$ , then subsequently detached by partial  $\text{SiO}_2$  etching<sup>67</sup>. The PMMA/graphene membrane was then placed over the target substrate and PMMA dissolved with acetone<sup>67</sup>. Kim *et al.* used a dry-method based on a polydimethylsiloxane stamp to transfer patterned films<sup>37</sup>. Bae *et al.* scaled the process to a roll-based layer-by-layer transfer onto plastic substrates<sup>39</sup>.

We have developed a procedure for deterministic placement, following transfer. This exploits a water layer between the PMMA/graphene foil and the substrate, which enables the PMMA to move. This allows us to place graphene layers on any substrate in any pre-defined location, prepare ‘artificial’ multilayers and create sandwich structures with other materials (such as BN or  $\text{MoS}_2$ ). We will show an example of this technique in the section entitled ‘Saturable absorbers and ultra-fast lasers’, by placing graphene on the core of an optical fibre.

Large-scale placement of LPE samples can be achieved by spin-coating and Langmuir–Blodgett techniques<sup>49</sup>. Surface modification by self-assembled monolayers can enable targeted deposition of graphene flakes on the large scale. Di-electrophoresis allows controlled placement of individual graphene flakes between pre-patterned electrodes<sup>68</sup>. Inkjet printing is another attractive technique<sup>69</sup>, and could directly ‘write’ optoelectronic devices or thin-film transistors.

## Photonics and optoelectronics applications

**Transparent conductors.** Optoelectronic devices such as displays, touch screens, light-emitting diodes and solar cells require materials with low sheet resistance  $R_s$  and high transparency. In a thin film,  $R_s = \rho/t$ , where  $t$  is the film thickness and  $\rho = 1/\sigma$  is the resistivity,  $\sigma$  being the d.c. conductivity. For a rectangle of length  $L$  and width  $W$ , the resistance  $R$  is:

$$R = \frac{\rho}{t} \times \frac{L}{W} = R_s \times \frac{L}{W}$$

The term  $L/W$  can be seen as the number of squares of side  $W$  that can be superimposed on the resistor without overlapping. Thus, even if  $R_s$  has units of ohms (as  $R$  does), it is historically quoted in ‘ohms per square’ ( $\Omega/\square$ ).

Current transparent conductors are semiconductor-based<sup>70</sup>: doped indium oxide ( $\text{In}_2\text{O}_3$ )<sup>71</sup>, zinc oxide ( $\text{ZnO}$ )<sup>72</sup> or tin oxide ( $\text{SnO}_2$ )<sup>70</sup>, as well as ternary compounds based on their combinations<sup>70,72,73</sup>. The dominant material is indium tin oxide (ITO), a doped n-type semiconductor composed of  $\sim 90\%$   $\text{In}_2\text{O}_3$  and  $\sim 10\%$   $\text{SnO}_2$  (ref. 70). The electrical and optical properties of ITO are strongly affected by impurities<sup>70</sup>. Tin atoms function as n-type donors<sup>70</sup>. ITO has strong absorption above 4 eV due to interband transitions<sup>70</sup>, with other features at lower energy related to scattering of free electrons by tin atoms or grain boundaries<sup>70</sup>. ITO is commercially available with  $T \approx 80\%$  and  $R_s$  as low as  $10 \Omega/\square$  on glass<sup>72</sup>, and  $\sim 60$ – $300 \Omega/\square$  on polyethylene terephthalate<sup>73</sup>. Note that  $T$  is typically quoted at 550 nm, as this is where the spectral response of the human eye is highest<sup>70</sup>.

ITO suffers severe limitations: an ever-increasing cost due to indium scarcity<sup>70</sup>, processing requirements, difficulties in patterning<sup>70,73</sup> and a sensitivity to both acidic and basic environments. Moreover, it is brittle and can easily wear out or crack when used in applications involving bending, such as touch screens and flexible displays<sup>74</sup>. This means that new transparent conductor materials are needed with improved performance. Metal grids<sup>75</sup>, metallic nanowires<sup>76</sup> or other metal oxides<sup>73</sup> have been explored as alternatives. Nanotubes and graphene also show great promise. In particular, graphene films have a higher  $T$  over a wider wavelength range than single-walled carbon nanotube (SWNT) films<sup>77–79</sup>, thin metallic films<sup>75,76</sup> and ITO<sup>70,72</sup> (Fig. 2a).

We now present a relation between  $T$  and  $R_s$  for FLG films of varying doping levels. From equation (3),  $T$  depends on the optical conductivity  $G_0$ :

$$T = \left( 1 + \frac{G_0}{2\varepsilon_0 c} N \right)^{-2} \quad (4)$$

where  $N$  is the number of layers. The sheet resistance  $R_s$  is linked to the bidimensional d.c. conductivity  $\sigma_{2D}$  by:

$$R_s = (\sigma_{2D} N)^{-1} \quad (5)$$

Combining equations (4) and (5) and eliminating  $N$  gives:

$$T = \left( 1 + \frac{Z_0}{2R_s} \frac{G_0}{\sigma_{2D}} \right)^{-2} \quad (6)$$

where  $Z_0 = 1/\varepsilon_0 c = 377 \Omega$  is the free-space impedance,  $\varepsilon_0$  is the



free-space electric constant and  $c$  is the speed of light. In graphene<sup>1</sup> we can take  $\sigma_{2D} = n\mu e$ , where  $n$  is the number of charge carriers. Note that for  $n \approx 0$ ,  $\sigma_{2D}$  does not go to zero, but assumes a constant value<sup>1</sup> of approximately  $4e^2/h$ , giving  $R_s \approx 6 \text{ k}\Omega/\square$  for an ideal intrinsic SLG with  $T \approx 97\%$ . Thus, an ideal intrinsic SLG would beat the best ITO only in terms of  $T$ , not  $R_s$ . However, real samples deposited on substrates, in thin films or embedded in polymers are never intrinsic. Exfoliated SLG typically has  $n \geq 10^{12} \text{ cm}^{-2}$  (see ref. 80, for example), and much smaller  $R_s$ . The range of  $T$  and  $R_s$  that can be realistically achieved for graphene layers of varying thickness can be estimated by taking  $n = 10^{12} - 10^{13} \text{ cm}^{-2}$  and  $\mu = 1,000 - 20,000 \text{ cm}^2 \text{ V}^{-1} \text{ s}^{-1}$ , which is typical for films grown by CVD. Figure 2b,c shows that graphene can achieve the same  $R_s$  as ITO, ZnO/Ag/ZnO (ref. 81), TiO<sub>2</sub>/Ag/TiO<sub>2</sub> and SWNTs with a similar or even higher  $T$ . Figure 2c plots  $T$  versus  $R_s$  for ITO (ref. 75), Ag nanowires<sup>75</sup>, SWNTs<sup>77</sup> and the best graphene-based transparent conductive films (TCFs) reported so far<sup>39</sup>, again showing that the latter is superior. For instance, taking  $n = 3.4 \times 10^{12} \text{ cm}^{-2}$  and  $\mu = 2 \times 10^4 \text{ cm}^2 \text{ V}^{-1} \text{ s}^{-1}$ , we get  $T = 90\%$  and  $R_s = 20 \Omega/\square$ .

Note that equation (6) is intended as a guideline for TCF design and optimization — not as a statement on the transport physics of graphene. For TCF design, empirical expressions of  $\sigma_{2D}$  as a function of carrier concentration and doping are enough, whatever the origin and precise quantification of the minimal conductivity, and of the dependence of  $R_s$  on doping, defects, electron-hole puddles and so on.

Different strategies were explored to prepare graphene-based TCFs (GTCFs): spraying<sup>82</sup>, dip<sup>83</sup> and spin coating<sup>84</sup>, vacuum filtration<sup>54</sup> and roll-to-roll processing<sup>39</sup>. Considerable progress has been made since the first attempts to produce graphene-oxide-based TCFs (GOTCFs). Because graphene oxide is insulating, it must be reduced to improve  $R_s$  (ref. 47). Gilje *et al.*<sup>82</sup> decreased  $R_s$  from  $40 \text{ G}\Omega/\square$  to  $4 \text{ M}\Omega/\square$  following reduction with dimethylhydrazine. Graphitization<sup>84</sup>, hydrazine exposure and low-temperature annealing<sup>54</sup>, or high-temperature vacuum annealing<sup>85</sup> further decreased  $R_s$  down to  $800 \Omega/\square$  for  $T = 82\%$  (ref. 85).

Dispersions of graphite-intercalated compounds<sup>86</sup> and hybrid nanocomposites (graphene oxide sheets mixed with silica sols or CNTs<sup>87</sup>) were also attempted, with a minimum  $R_s = 240 \Omega/\square$  for  $T = 86\%$  (ref. 87). Graphene films produced by chemical synthesis currently show  $R_s = 1.6 \text{ k}\Omega/\square$  for  $T = 55\%$  (ref. 65).

Blake *et al.*<sup>88</sup> have reported the best GTCF so far, from LPE of graphite. This was fabricated by vacuum filtration followed by annealing, achieving  $R_s = 5 \text{ k}\Omega/\square$  and  $T \approx 90\%$ . The high  $R_s$  is most likely due to the small flake size and lack of percolation<sup>48,88</sup>. The role of percolation can be seen in ref. 48, where  $R_s$  and  $T$  went from  $6 \text{ k}\Omega/\square$  and  $\sim 75\%$ , to  $2 \text{ k}\Omega/\square$  and  $\sim 77\%$  with increasing flake size.

A key strategy to improving performance is stable chemical doping. Blake *et al.*<sup>88</sup> prepared GTCFs, produced by micromechanical cleavage, with  $T \approx 98\%$  and  $R_s = 400 \Omega/\square$ , using a layer of polyvinyl alcohol to induce n-type doping. Bae *et al.*<sup>39</sup> achieved  $R_s \approx 30 \Omega/\square$  and  $T \approx 90\%$  by nitric acid treatment of GTCFs derived from CVD-grown flakes — one order of magnitude lower in terms of  $R_s$  than previous GTCFs from the wet transfer of CVD films<sup>37</sup>.

Figure 2d is an overview of current GTCFs and GOTCFs. It shows that GTCFs derived from CVD flakes, combined with doping, could outperform ITO, metal wires and SWNTs. Note that GTCFs and GOTCFs produced by other methods, such as LPE, although currently having higher  $R_s$  at  $T = 90\%$ , have already been tested in organic light emitters<sup>85,89</sup> and solar cells<sup>83,90</sup>. These are cheaper and easier to scale than micromechanical cleavage or CVD films, and must be considered for applications in which cost reduction is crucial.

**Photovoltaic devices.** A photovoltaic cell converts light to electricity<sup>91</sup>. The energy conversion efficiency is  $\eta = P_{\text{max}}/P_{\text{inc}}$ , where  $P_{\text{max}} = V_{\text{OC}} \times I_{\text{SC}} \times \text{FF}$  and  $P_{\text{inc}}$  is the incident power. Here,  $I_{\text{SC}}$  is the

maximum short-circuit current,  $V_{\text{OC}}$  is the maximum open-circuit voltage and FF is the fill factor, defined as  $\text{FF} = (V_{\text{max}} \times I_{\text{max}})/(V_{\text{OC}} \times I_{\text{SC}})$ , where  $V_{\text{max}}$  and  $I_{\text{max}}$  are the maximum voltage and current, respectively. The fraction of absorbed photons converted to current defines the internal photocurrent efficiency.

Current photovoltaic technology is dominated by silicon cells<sup>91</sup>, with  $\eta$  up to  $\sim 25\%$  (ref. 92). Organic photovoltaic cells rely on polymers for light absorption and charge transport<sup>93</sup>. They can be manufactured economically compared with silicon cells, for example by a roll-to-roll process<sup>94</sup>, even though they have lower  $\eta$ . An organic photovoltaic cell consists of a transparent conductor, a photoactive layer and the electrode<sup>93</sup>. Dye-sensitized solar cells use a liquid electrolyte as a charge-transport medium<sup>95</sup>. This type of solar cell consists of a high-porosity nanocrystalline photoanode, comprising TiO<sub>2</sub> and dye molecules, both deposited on a transparent conductor<sup>95</sup>. When illuminated, the dye molecules capture the incident photon, generating electron-hole pairs. The electrons are injected into the conduction band of the TiO<sub>2</sub> and are then transported to the counter-electrode<sup>95</sup>. Dye molecules are regenerated by capturing electrons from a liquid electrolyte. At present, ITO is the most common material for use both as a photoanode and cathode, the latter with a platinum coating.

Graphene can fulfil multiple functions in photovoltaic devices: as the transparent conductor window, photoactive material, channel for charge transport, and catalyst. GTCFs can be used as window electrodes in inorganic (Fig. 3a), organic (Fig. 3b) and dye-sensitized solar cell devices (Fig. 3c). Wang *et al.* used GTCFs produced by chemical synthesis, reporting  $\eta \approx 0.3\%$  (ref. 65). A higher  $\eta$  of  $\sim 0.4\%$  was achieved using reduced graphene oxide<sup>96</sup>, with  $R_s = 1.6 \text{ k}\Omega/\square$  instead of  $5 \text{ k}\Omega/\square$  (ref. 65), despite a lower  $T$  ( $55\%$  instead of  $80\%$ ). De Arco *et al.* achieved better performance ( $\eta \approx 1.2\%$ ) using CVD graphene as the transparent conductor, with  $R_s = 230 \Omega/\square$  and  $T = 72\%$  (ref. 97). Further optimization is certainly possible, considering the performance of the best GTCF so far<sup>39</sup>.

Graphene oxide dispersions were also used in bulk-heterojunction photovoltaic devices, as electron-acceptors with poly(3-hexylthiophene) and poly(3-octylthiophene) as donors, achieving  $\eta \approx 1.4\%$  (ref. 90). Yong *et al.* claim that  $\eta > 12\%$  should be possible with graphene as photoactive material<sup>98</sup>.

Graphene can cover an even larger number of functions in dye-sensitized solar cells. Wang *et al.* reported a solid-state solar cell based on the organic compound spiro-OMeTAD1 (as the hole transport material) and porous TiO<sub>2</sub> (for electron transport) using a GTCF anode, with  $\eta \approx 0.26\%$  (ref. 83). Graphene can be incorporated into the nanostructured TiO<sub>2</sub> photoanode to enhance the charge transport rate, preventing recombination, thus improving the internal photocurrent efficiency<sup>99</sup>. Yang *et al.* used graphene as a TiO<sub>2</sub> bridge, achieving faster electron transport and lower recombination, and leading to  $\eta \approx 7\%$ , which is higher than they achieved with conventional nanocrystalline TiO<sub>2</sub> photoanodes in the same experimental conditions<sup>99</sup>. Another option is to use graphene, with its high specific surface area, to substitute for the platinum counter-electrode. A hybrid poly(3,4-ethylenedioxythiophene):poly(styrenesulphonate) (PEDOT:PSS)/graphene oxide composite was used as counter-electrode, to obtain  $\eta = 4.5\%$ , comparable to the  $6.3\%$  for a platinum counter-electrode tested under the same conditions<sup>100</sup> but now with a cheaper material.

**Light-emitting devices.** Organic light-emitting diodes (OLEDs) have an electroluminescent layer between two charge-injecting electrodes, at least one of which is transparent<sup>101</sup>. In these diodes, holes are injected into the highest occupied molecular orbital (HOMO) of the polymer from the anode, and electrons are injected into the lowest unoccupied molecular orbital (LUMO) from the cathode. For efficient injection, the anode and cathode work functions should match the HOMO and LUMO of the light-emitting polymer<sup>101</sup>. Because of their high image quality, low power consumption and

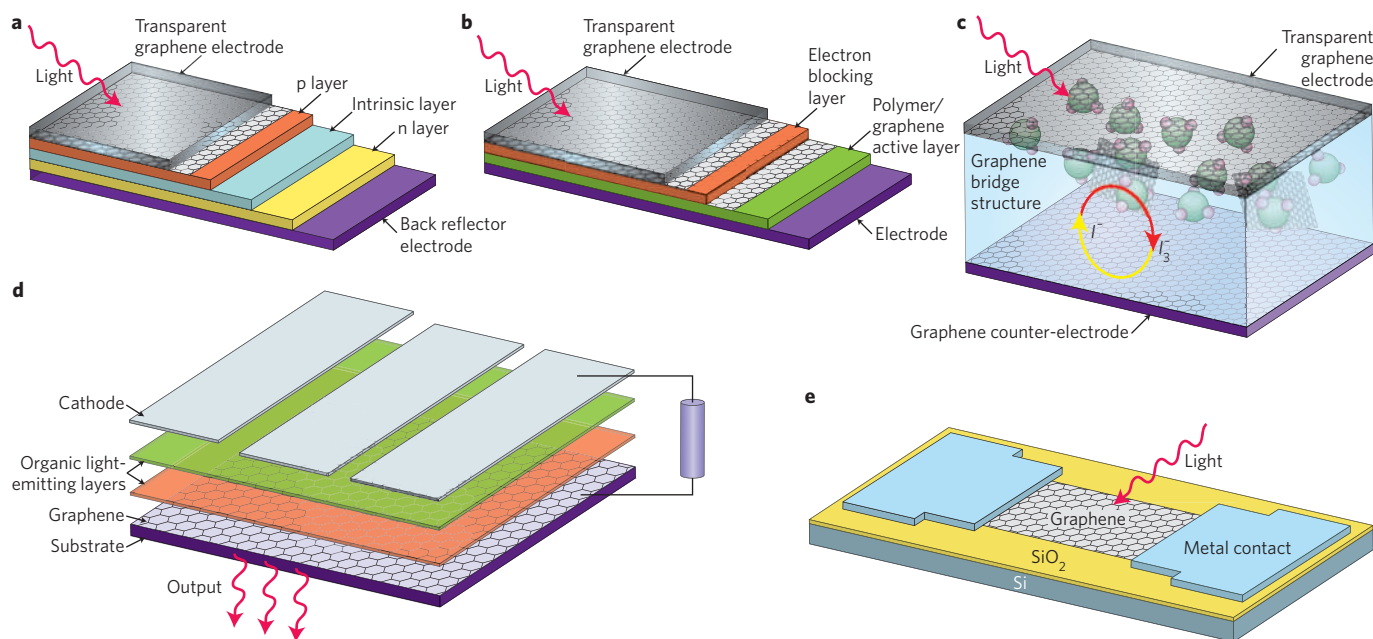


**Figure 3 | Graphene-based optoelectronics.** **a–c**, Schematics of inorganic (**a**), organic (**b**) and dye-sensitized (**c**) solar cells.  $I^-$  and  $I_3^-$  are iodide and tri-iodide, respectively. The  $I^-$  and  $I_3^-$  ions transfer electrons to the oxidized dye molecules, thus completing the internal electrochemical circuit between the photoanode and the counter-electrode. **d,e**, Schematics of an organic LED (**d**) and a photodetector (**e**). The cylinder in **d** represents an applied voltage.

ultrathin device structure, OLEDs find applications in ultrathin televisions and other display screens such as computer monitors, digital cameras and mobile phones. Traditionally, ITO, with its work function of 4.4–4.5 eV, is used as the transparent conductive film. However, besides cost issues, ITO is brittle and limited as a flexible substrate<sup>73</sup>. In addition, indium tends to diffuse into the active OLED layers, which reduces device performance over time<sup>70</sup>. Thus, there is a need for alternative TCFs with optical and electrical performance similar to ITO, but without its drawbacks. Graphene has a work function of 4.5 eV, similar to ITO. This, combined with its promise as a flexible and cheap TCF, makes it an ideal candidate for an OLED anode (Fig. 3d), while also eliminating the issues related to indium diffusion. GTCFs anodes enable an out-coupling efficiency comparable to ITO<sup>85</sup>. Considering that the  $R_s$  and  $T$  of ref. 85 were 800  $\Omega/\square$  and 82% at 550 nm, it is reasonable to expect that further optimization will improve performance.

Matyba *et al.*<sup>89</sup> used a GOTCF in a light-emitting electrochemical cell. Similar to an OLED, this is a device in which the light-emitting polymer is blended with an electrolyte<sup>102</sup>. The mobile ions in the electrolyte rearrange when a potential is applied between the electrodes, forming layers with high charge density at each electrode interface, which allows efficient and balanced injection of electrons and holes, regardless of the work function of the electrodes<sup>102</sup>. Usually, the cells have at least one metal electrode. Electrochemical side-reactions, involving the electrode materials, can cause problems in terms of operational lifetime and efficiency<sup>89</sup>. This also hinders the development of flexible devices. Graphene is the ideal material to overcome these problems. Matyba *et al.*<sup>89</sup> demonstrated a light-emitting electrochemical cell based solely on dispersion-processable carbon-based materials, paving the way towards totally organic low-voltage, inexpensive and efficient LEDs.

**Photodetectors.** Photodetectors measure photon flux or optical power by converting the absorbed photon energy into electrical current. They are widely used in a range of common devices<sup>103</sup>, such as remote controls, televisions and DVD players. Most exploit the internal photoeffect, in which the absorption of photons results in carriers excited from the valence to the conduction band, outputting

an electric current. The spectral bandwidth is typically limited by the material's absorption<sup>103</sup>. For example, photodetectors based on IV and III–V semiconductors suffer from the 'long-wavelength limit', as these become transparent when the incident energy is smaller than the bandgap<sup>103</sup>. Graphene absorbs from the ultraviolet to terahertz range<sup>11,13,104,105</sup>. As a result, graphene-based photodetectors (GPDs; see Fig. 3e) could work over a much broader wavelength range. The response time is ruled by the carrier mobility<sup>103</sup>. Graphene has huge mobilities, so GPDs can be ultrafast.

The photoelectrical response of graphene has been widely investigated both experimentally and theoretically<sup>106–110</sup>. Responses at wavelengths of 0.514, 0.633, 1.5 and 2.4  $\mu\text{m}$  have been reported<sup>110</sup>. Much broader spectral detection is expected because of the graphene ultrawideband absorption. Xia *et al.* demonstrated a GPD with a photoreponse of up to 40 GHz (ref. 109). The operating bandwidth of GPDs is mainly limited by their time constant resulting from the device resistance,  $R$ , and capacitance,  $C$ . Xia *et al.* reported an RC-limited bandwidth of about 640 GHz (ref. 109), which is comparable to traditional photodetectors<sup>111</sup>. However, the maximum possible operating bandwidth of photodetectors is typically restricted by their transit time, the finite duration of the photogenerated current<sup>103</sup>. The transit-time-limited bandwidth of a GPD could be well over 1,500 GHz (ref. 109), surpassing state-of-the-art photodetectors.

Although an external electric field can produce efficient photocurrent generation with an electron–hole separation efficiency of over 30% (ref. 107), zero source–drain bias and dark current operations could be achieved by using the internal electric field formed near the metal electrode–graphene interfaces<sup>109,110</sup>. However, the small effective area of the internal electric field could decrease the detection efficiency<sup>109,110</sup>, as most of the generated electron–hole pairs would be out of the electric field, thus recombining, rather than being separated. The internal photocurrent efficiencies (15–30%; refs 107,108) and external responsivity (generated electric current for a given input optical power) of  $\sim 6.1$  mA per watt so far reported<sup>110</sup> for GPDs are relatively low compared with current photodetectors<sup>103</sup>. This is mainly due to limited optical absorption when only one SLG is used, short photocarrier lifetimes and small effective photodetection areas ( $\sim 200$  nm in ref. 109).

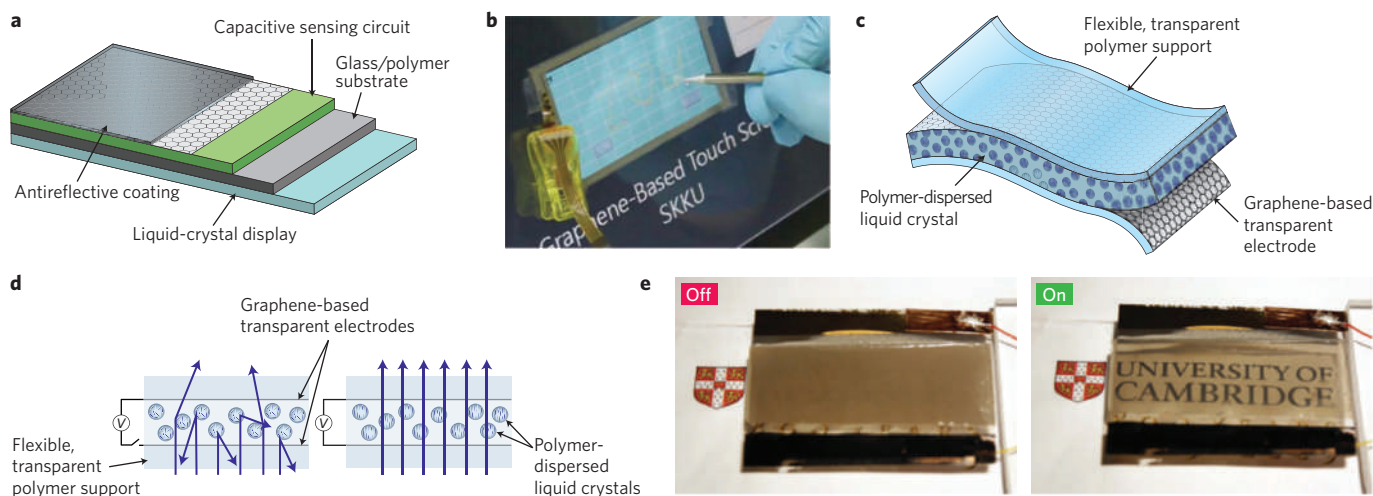


**Figure 4 | Graphene touch screen and smart window.** **a**, Schematic of a capacitive touch screen. **b**, Resistive graphene-based touch screen. **c**, Schematic of a PDLC smart window using a GTCF. **d**, With no voltage, the liquid-crystal molecules are not aligned, making the window opaque. **e**, Graphene/nanotube-based smart window in either an off (left) or on (right) state. Image in **b** reproduced with permission from ref. 39, © 2010 NPG.

The photothermoelectric effect, which exploits the conversion of photon energy into heat and then electric signal<sup>103</sup>, may play an important part in photocurrent generation in graphene devices<sup>107,112</sup>. Thus photothermoelectric GPDs may be possible.

**Touch screens.** Touch screens are visual outputs that can detect the presence and location of a touch within the display area, permitting physical interaction with what is shown on the display itself<sup>113</sup>. Touch panels are currently used in a wide range of applications such as cellular phones and digital cameras because they allow quick, intuitive and accurate interaction by the user with the display content.

Resistive and capacitive touch panels are the most common (Fig. 4a). A resistive touch panel comprises a conductive substrate, a liquid-crystal device front panel and a TCF<sup>113</sup>. When pressed, the front-panel film comes into contact with the bottom TCF, and the coordinates of the contact point are calculated on the basis of their resistance values. There are two categories of resistive touch screens: matrix and analogue<sup>113</sup>. The matrix has striped electrodes, whereas the analogue has a non-patterned transparent conductive electrode with lower production costs. The TCF requirements for resistive screens are  $R_s \approx 500\text{--}2,000\ \Omega/\square$  and  $T > 90\%$  at 550 nm (ref. 113). Favourable mechanical properties, including brittleness and wear resistance, high chemical durability, no toxicity and low production costs, are also important. Cost, brittleness, wear resistance and chemical durability are the main limitations of ITO<sup>70,73</sup>, which cannot withstand the repeated flexing and poking involved with this type of application. Thus, for resistive touch screens there is an effort to find an alternative transparent conductor.

GTCFs can satisfy the requirements for resistive touch screens in terms of  $T$  and  $R_s$ , as well as exhibiting large-area uniformity. Bae *et al.*<sup>39</sup> recently produced a graphene-based touch panel display by screen-printing a CVD-grown sample (Fig. 4b). Considering the  $R_s$  and  $T$  required by analogue resistive screens, GTCFs or GOTCFs produced by LPE are also viable alternatives, further reducing costs.

Capacitive touch screens are emerging as the high-end technology, especially since the launch of Apple's iPhone. These consist of an insulator such as glass, coated with ITO<sup>113</sup>. As the human body is also a conductor, touching the surface of the screen results in an electrostatic field distortion, which is measurable as a change in capacitance. Although capacitive touch screens do not work by poking with a pen (making mechanical stresses lower than for resistive screens), the use of GTCFs can still improve performance and reduce costs.

**Flexible smart windows and bistable displays.** Polymer-dispersed liquid-crystal (PDLC) devices were introduced in the early 1980s<sup>114</sup>. These consist of thin films of optically transparent polymers with micrometre-sized liquid-crystal droplets contained within pores of the polymer. Light passing through the liquid-crystal/polymer is strongly scattered, producing a milky film. If the liquid crystal's ordinary refractive index is close to that of the host polymer, applying an electric field results in a transparent state<sup>74</sup>. In principle, any type of thermotropic liquid crystal may be used in PDLC devices for applications not requiring high switching speeds. In particular, the ability to switch from translucent to opaque makes them attractive for electrically switchable 'smart windows' that can be activated when privacy is required. Conventionally, ITO on glass is used as the conductive layer to apply the electric field across the PDLC. However, one of the reasons behind the limited market penetration of smart windows is the high cost of ITO. Furthermore, flexibility is hindered when using ITO, reducing potential applications such as PDLC flexible displays<sup>74</sup>. Transparent or coloured/tinted smart windows generally require  $T$  to be 60–90% or higher and  $R_s$  to be 100–1,000  $\Omega/\square$ , depending on production cost, application and manufacturer. In addition to flexibility, the electrodes need to be as large as the window itself and must have long-term physical and chemical stability, as well as being compatible with the roll-to-roll PDLC production process. Liquid crystals could also be used for next-generation zero-power monochromatic and coloured flexible bistable displays, which can retain an image with no power consumption. These are attractive for signs and advertisements or for e-readers, and require a transparent flexible conductor for switching the image. The present ITO devices are not ideal for this application, owing to the limitations discussed above.

All these deficiencies of ITO electrodes can be overcome by GTCFs. Figure 4c,d shows their working principle, and Fig. 4e shows a prototype of a flexible smart window with polyethylene terephthalate used as a substrate.

**Saturable absorbers and ultrafast lasers.** Materials with nonlinear optical and electro-optical properties are needed in most photonic applications. Laser sources producing nano- to subpicosecond pulses are a key component in the portfolio of leading laser manufacturers. Solid-state lasers have so far been the short-pulse source of choice, being deployed in applications ranging from basic research to materials processing, from eye surgery and printed circuit-board manufacturing to metrology and the trimming of electronic



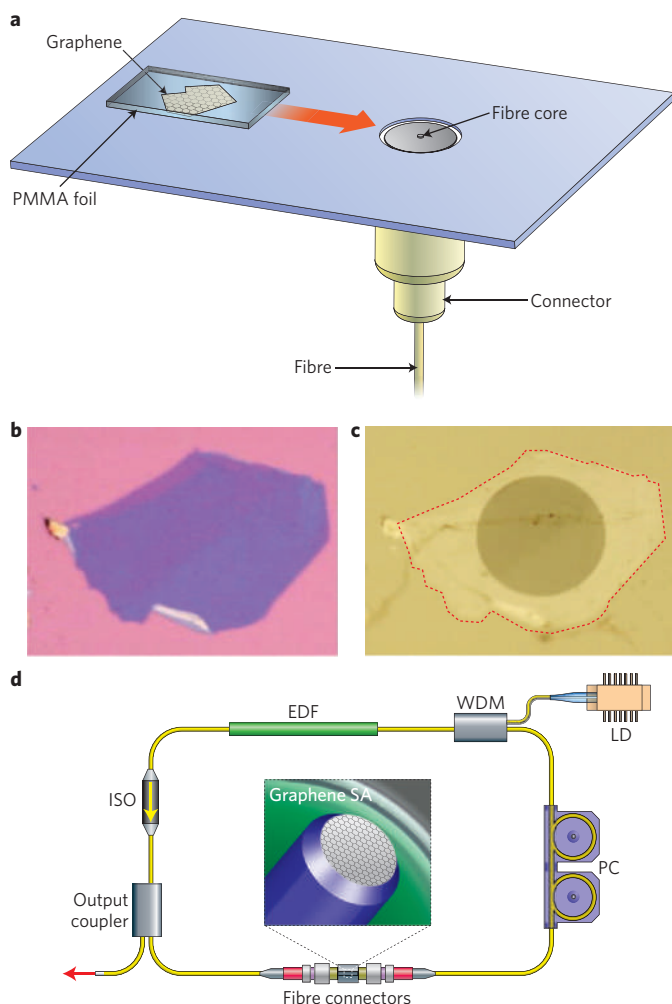


**Figure 5 | Graphene integration in fibre lasers.** **a**, An optical fibre is mounted onto a holder. Once detached from the original substrate, a polymer/graphene membrane is slid and aligned with the fibre core. **b**, Flake originally deposited on  $\text{SiO}_2/\text{Si}$ . **c**, The same flake after deterministic placement and dissolution of the polymer layer. **d**, Graphene mode-locked ultrafast laser: a graphene saturable absorber (SA) is inserted between two fibre connectors. An erbium-doped fibre (EDF) is the gain medium, pumped by a laser diode (LD) with a wavelength-division multiplexer (WDM). An isolator (ISO) maintains unidirectional operation, and a polarization controller (PC) optimizes mode-locking.

components such as resistors and capacitors. Regardless of wavelength, the majority of ultrafast laser systems use a mode-locking technique, whereby a nonlinear optical element, called a saturable absorber, turns the continuous-wave output into a train of ultrafast optical pulses<sup>115</sup>. The key requirements for nonlinear materials are fast response time, strong nonlinearity, broad wavelength range, low optical loss, high power handling, low power consumption, low cost and ease of integration into an optical system. Currently, the dominant technology is based on semiconductor saturable absorber mirrors<sup>115</sup>. However, these have a narrow tuning range, and require complex fabrication and packaging<sup>12,115</sup>. A simple, cost-effective alternative is to use SWNTs<sup>12,116</sup>, in which the diameter controls the gap and thus the operating wavelength. Broadband tunability is possible using SWNTs with a wide diameter distribution<sup>12,116</sup>. However, when operating at a particular wavelength, SWNTs not in resonance are not used and contribute unwanted losses.

As discussed above, the linear dispersion of the Dirac electrons in graphene offers an ideal solution: for any excitation there is always an

electron-hole pair in resonance. The ultrafast carrier dynamics<sup>25,117</sup>, combined with large absorption and Pauli blocking, make graphene an ideal ultrabroadband, fast saturable absorber. Unlike semiconductor saturable absorber mirrors and SWNTs, there is no need for band-gap engineering or chirality/diameter control.

So far, graphene-polymer composites<sup>12,13,118–120</sup>, CVD-grown films<sup>121,122</sup>, functionalized graphene (for example, graphene oxide bonded with poly(m-phenylenevinylene-co-2,5-dioctoxy-p-phenylenevinylene)<sup>119</sup> and reduced graphene oxide flakes<sup>123,124</sup> have been used for ultrafast lasers. Graphene-polymer composites are scalable and, more importantly, easily integrated into a range of photonic systems<sup>12,13,118</sup>. Another route for graphene integration is by deterministic placement in a pre-defined position on a substrate of choice, for example a fibre core or cavity mirrors. Figure 5a shows the transfer of such a flake onto an optical fibre core. This is achieved by using a water layer between the PMMA/graphene foil and the optical fibre, which enables the PMMA to move. Graphene device integration is finally achieved after precise alignment to the optical fibre core by a micromanipulator (Fig. 5b) and dissolution of the PMMA layer (Fig. 5c).

A typical absorption spectrum is shown in Fig. 6a<sup>12,13,118</sup>. This is featureless apart from the characteristic ultraviolet peak, and the host polymer only contributes a small background for longer wavelengths. Figure 6b plots  $T$  as a function of average pump power for six wavelengths. Saturable absorption is evident from the  $T$  increase with power at all wavelengths.

Various strategies have been proposed to integrate graphene saturable absorbers (GSAs) in laser cavities for ultrafast pulse generation. The most common is to sandwich a GSA between two fibre connectors with a fibre adaptor, as shown schematically in Fig. 5d<sup>12,13,118</sup>. Graphene on a side-polished fibre has also been reported, aimed at high power generation by evanescent field interaction<sup>123</sup>. A quartz substrate coated with graphene has been used for free-space solid-state lasers<sup>124</sup>.

The most common wavelength of generated ultrafast pulses so far is  $\sim 1.5 \mu\text{m}$ , not because GSAs have any preference for a particular wavelength, but because this is the standard wavelength of optical telecommunications. A solid-state laser mode-locked by graphene has been reported at  $\sim 1 \mu\text{m}$  (ref. 124). Figure 6c shows a GSA mode-locked laser, made from erbium-doped fibre and tunable from 1,526 to 1,559 nm, with the tuning range mainly limited by the tunable filter, not the GSA<sup>118</sup>. Figure 6d,e shows the pulse from a graphene-oxide-based saturable absorber. The possibility of tuning the GSA properties by functionalization or by using different layers or composite concentrations offers considerable design freedom. Table 1 gives a performance comparison of graphene-based ultrafast lasers and the main carbon-nanotube-based devices<sup>125,126</sup>.

**Optical limiters.** Optical limiters are devices that have high transmittance for low incident light intensity, and low transmittance for high intensity<sup>127</sup>. There is a great interest in these for optical sensors and human eye protection, as retinal damage can occur when intensities exceed a certain threshold<sup>127</sup>. Passive optical limiters, which use a nonlinear optical material, have the potential to be simple, compact and cheap<sup>127</sup>. However, so far no passive optical limiters have been able to protect eyes and other common sensors over the entire visible and near-infrared range<sup>127</sup>. Typical materials include semiconductors (for example ZnSe, InSb), organic molecules (for example phthalocyanines), liquid crystals and carbon-based materials (for example, carbon-black dispersions, CNTs and fullerenes)<sup>127,128</sup>. Fullerenes and their derivatives<sup>129,130</sup> and CNT dispersions<sup>130</sup> have good optical limiting performance, in particular for nanosecond pulses at 532 and 1,064 nm (ref. 130).

In graphene-based optical limiters the absorbed light energy converts into heat, creating bubbles and microplasmas<sup>128</sup>, which results in reduced transmission. Graphene dispersions can be used as



wideband optical limiters covering visible and near-infrared. Broad optical limiting (at 532 and 1,064 nm) by LPE graphene was reported for nanosecond pulses<sup>128</sup>. It has also been shown<sup>131</sup> that functionalized graphene dispersions could outperform  $C_{60}$  as an optical limiter.

**Optical frequency converters.** Optical frequency converters are used to expand the wavelength accessibility of lasers (for example, frequency doubling, parametric amplification and oscillation, and four-wave mixing)<sup>127</sup>. Calculations suggest that nonlinear frequency generation in graphene (harmonics of input light, for example) should be possible for sufficiently high external electric fields ( $>100 \text{ V cm}^{-1}$ )<sup>132</sup>. Second-harmonic generation from a 150 fs laser at 800 nm has been reported for a graphene film<sup>133</sup>. In addition, four-wave mixing to generate near-infrared wavelength tunable light has been demonstrated using SLG and FLG<sup>134</sup>. Graphene's third-order susceptibility  $|\chi^3|$  was measured to be  $\sim 10^{-7}$  e.s.u. (ref. 134) — up to one order of magnitude larger than that reported so far for similar measurements on CNTs<sup>134</sup>. However, photon-counting electronics is typically needed to measure the output<sup>133</sup>, indicating a low conversion efficiency. Other features of graphene, such as the possibility of tuning the nonlinearity by changing the number of layers<sup>134</sup>, and wavelength-independent nonlinear susceptibility<sup>134</sup>, still could be potentially used for various photonic applications (optical imaging<sup>134</sup>, for example).

**Terahertz devices.** Radiation in the 0.3–10 THz range (30  $\mu\text{m}$  to 1 mm) is attractive for biomedical imaging, security, remote sensing and spectroscopy<sup>135</sup>. Much unexplored territory still remains for terahertz technology, mainly owing to a lack of affordable and efficient sources and detectors<sup>135</sup>. The frequency of graphene plasma waves<sup>136</sup> lies in the terahertz range, as well as the gap of graphene nanoribbons, and the bilayer graphene tunable band-gap, making graphene appealing for terahertz generation and detection. Various terahertz sources have been suggested based on electrical<sup>136</sup> or optical<sup>136</sup> pumping of graphene devices. Recent experimental observations of terahertz emission<sup>137</sup> and amplification<sup>138</sup> in optically pumped graphene have shown the feasibility of graphene-based terahertz generation. Twisted multilayers, retaining the electronic properties of SLG, could also be very interesting for such applications.

Graphene devices can be used for terahertz detection and frequency conversion. The possibility of tuning the electronic and optical properties by external means (for example through electric or magnetic fields, or using an optical pump) makes SLG and FLG suitable for infrared and terahertz radiation manipulation. The possible devices include modulators, filters, switches, beamsplitters and polarizers.

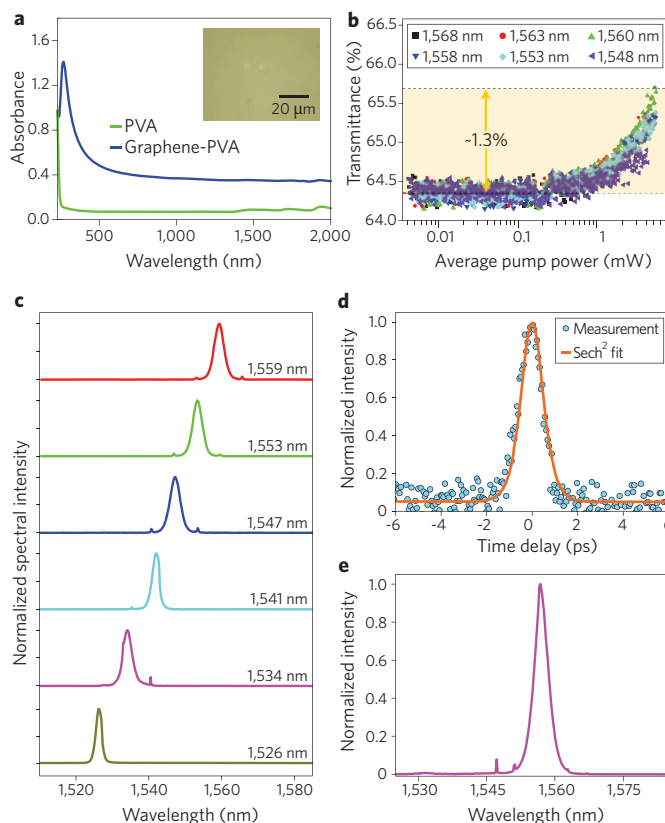


**Figure 6 | Graphene mode-locked laser performance.** **a**, Absorption of graphene-PVA (polyvinyl alcohol) composite and reference PVA. Inset: micrograph of the composite. **b**, Typical transmittance as a function of pump power at six different wavelengths. Transmittance increases with power. **c**, Tunable ( $>30 \text{ nm}$ ) fibre laser mode-locked by graphene. **d,e**, Autocorrelation (**d**) and spectrum (**e**) of output pulses of a graphene oxide mode-locked laser, with a  $\sim 743 \text{ fs}$  pulse duration. Figure **a,b** reproduced with permission from ref. 13, © 2010 ACS.

## Perspective

Graphene films and composites have ideal electronic and optical properties for photonics and optoelectronics. Graphene is an attractive replacement for ITO and other transparent conductors. In many cases (touch screens or OLEDs, for example), this increases fabrication flexibility, in addition to having economic advantages. Present

**Table 1 | Graphene-based mode-locked lasers**

Laser type	Coupling method	Fabrication type	Laser parameters				Reference
			Wavelength ( $\lambda$ )	Pulse width ( $\tau$ )	Frequency	Power	
EDFL	Sandwiching	LPE	1,557 nm	800 fs	—	—	12
			1,559 nm	464 fs	19.9 MHz	—	13
			1,525–1,559 nm	1 ps	8 MHz	1 mW	118
	Sandwiching	CVD	1,565 nm	756 fs	1.79 MHz	2 mW	119
			1,576 nm	415 fs	6.84 MHz	50 mW	121
			1,570–1,600 nm	40–140 ps	1.5 MHz	—	122
			1,570–1,600 nm	1.08 ps	6.95 MHz	—	119
	Sandwiching	FG	1,590 nm	700 fs	6.95 MHz	50 mW	120
			1,561 nm	1.3 ps	6.99 MHz	51 mW	123
Nd:YAG	Free space	RGO	1,064 nm	4 ps	88 MHz	0.1 W	124
—	—	CNT	1–2 $\mu\text{m}$	68 fs–2 ns	177 kHz–17 GHz	1.6 W	12,116,125,126

EDFL, erbium-doped fibre laser; FG, functionalized graphene; Nd:YAG, neodymium-doped yttrium aluminium garnet solid-state laser.

liquid-crystal-based devices face high fabrication costs associated with the requirement for large transparent electrodes. The move to a graphene-based technology could make them more viable. New forms of graphene-based transparent electrodes on flexible substrates for solar cells can add value and a level of operational flexibility that is not possible with current transparent conductors and rigid glass substrates. Recent progress in growth and dispersion processing of graphene have definitely made this material 'come of age', thus encouraging industrial applications. Deterministic placement of graphene layers on arbitrary substrates, and the creation of multilayers by the individual assembly of monolayers at given angles, are now possible. Future efforts in the field of nonlinear optical devices will focus on demonstrators at different wavelengths to make full use of graphene's ultrawide broadband capability. This could include high-speed, transparent and flexible photosensitive systems, which could be further functionalized to enable chemical sensing. Ultrafast and tunable lasers have become a reality, with an ever-growing number of groups entering this field. The combination of graphene photonics with plasmonics could lead to a wide range of advanced devices.

## References

- Geim, A. K. & Novoselov, K. S. The rise of graphene. *Nature Mater.* **6**, 183–191 (2007).
- Charlier, J. C., Eklund, P. C., Zhu, J. & Ferrari, A. C. Electron and phonon properties of graphene: Their relationship with carbon nanotubes. *Top. Appl. Phys.* **111**, 673–709 (2008).
- Wallace, P. R. The band theory of graphite. *Phys. Rev.* **71**, 622–634 (1947).
- Zhang, Y., Tan, Y.-W., Stormer, H. L. & Kim, P. Experimental observation of the quantum Hall effect and Berry's phase in graphene. *Nature* **438**, 201–204 (2005).
- Du, X. I. *et al.* Fractional quantum Hall effect and insulating phase of Dirac electrons in graphene. *Nature* **462**, 192–195 (2009).
- Lemme, M. C., Echtermeyer, T. J., Baus, M. & Kurz, H. A graphene field-effect device. *IEEE Electr. Device Lett.* **28**, 282–284 (2007).
- Han, M. Y., Ozyilmaz, B., Zhang, Y. & Kim, P. Energy band-gap engineering of graphene nanoribbons. *Phys. Rev. Lett.* **98**, 206805 (2007).
- Lin, Y.-M. *et al.* 100-GHz transistors from wafer-scale epitaxial graphene. *Science* **327**, 662 (2010).
- Casiraghi, C. *et al.* Raman imaging of graphene and graphene layers. *Nano Lett.* **7**, 2711–2717 (2007).
- Blake, P. *et al.* Making graphene visible. *Appl. Phys. Lett.* **91**, 063124 (2007).
- Nair, R. R. *et al.* Fine structure constant defines transparency of graphene. *Science* **320**, 1308–1308 (2008).
- Hasan, T. *et al.* Nanotube–polymer composites for ultrafast photonics. *Adv. Mater.* **21**, 3874–3899 (2009).
- Sun, Z. *et al.* Graphene mode-locked ultrafast laser. *ACS Nano* **4**, 803–810 (2010).
- Stoehr, R. J., Kolesov, R., Pflaum, J. & Wrachtrup, J. Fluorescence of laser created electron–hole plasma in graphene. Preprint at <http://arxiv.org/abs/1006.5434v1> (2010).
- Liu, C. H., Mak, K. F., Shan, J. & Heinz, T. F. Ultrafast photoluminescence from graphene. Preprint at <http://arxiv.org/abs/1006.5769v1> (2010).
- Wu, S. *et al.* Nonlinear photoluminescence from graphene. Abstract number: BAPS.2010.MAR.Z22.11, APS March Meeting, Portland, Oregon (2010).
- Hartschuh, A. *et al.* Excited state energies and decay dynamics in carbon nanotubes and graphene. E-MRS Spring Meeting (2010).
- Gokus, T. *et al.* Making graphene luminescent by oxygen plasma treatment. *ACS Nano* **3**, 3963–3968 (2009).
- Eda, G. *et al.* Blue photoluminescence from chemically derived graphene oxide. *Adv. Mater.* **22**, 505–509 (2009).
- Sun, X. *et al.* Nano-graphene oxide for cellular imaging and drug delivery. *Nano Res.* **1**, 203–212 (2008).
- Luo, Z., Vora, P. M., Mele, E. J., Johnson, A. T. & Kikkawa, J. M. Photoluminescence and band gap modulation in graphene oxide. *Appl. Phys. Lett.* **94**, 111909 (2009).
- Kuzmenko, A. B., van Heumen, E., Carbone, F. & van der Marel, D. Universal optical conductance of graphite. *Phys. Rev. Lett.* **100**, 117401 (2008).
- Wang, F. *et al.* Gate-variable optical transitions in graphene. *Science* **320**, 206–209 (2008).
- Mak, K. F., Shan, J. & Heinz, T. F. Electronic structure of few-layer graphene: experimental demonstration of strong dependence on stacking sequence. *Phys. Rev. Lett.* **104**, 176404 (2009).
- Breusing, M., Ropers, C. & Elsaesser, T. Ultrafast carrier dynamics in graphite. *Phys. Rev. Lett.* **102**, 086809 (2009).
- Kampf, T., Perfetti, L., Schapper, F., Frischkorn, C. & Wolf, M. Strongly coupled optical phonons in the ultrafast dynamics of the electronic energy and current relaxation in graphite. *Phys. Rev. Lett.* **95**, 187403 (2005).
- Lazzeri, M., Piscanec, S., Mauri, F., Ferrari, A. C. & Robertson, J. Electronic transport and hot phonons in carbon nanotubes. *Phys. Rev. Lett.* **95**, 236802 (2005).
- González, J., Guinea, F. & Vozmediano, M. A. H. Unconventional quasiparticle lifetime in graphite. *Phys. Rev. Lett.* **77**, 3589–3592 (1996).
- Lu, J. *et al.* One-pot synthesis of fluorescent carbon nanoribbons, nanoparticles, and graphene by the exfoliation of graphite in ionic liquids. *ACS Nano* **3**, 2367–2375 (2009).
- Sheats, J. R. *et al.* Organic electroluminescent devices. *Science* **273**, 884–888 (1996).
- Rothberg, L. J. & Lovinger, A. J. Status of and prospects for organic electroluminescence. *J. Mater. Res.* **11**, 3174–3187 (1996).
- Frangioni, J. V. *In vivo* near-infrared fluorescence imaging. *Curr. Opin. Chem. Biol.* **7**, 626–634 (2003).
- Essig, S. *et al.* Phonon-assisted electroluminescence from metallic carbon nanotubes and graphene. *Nano Lett.* **10**, 1589–1594 (2010).
- Novoselov, K. S. *et al.* Two-dimensional atomic crystals. *Proc. Natl Acad. Sci. USA* **102**, 10451–10453 (2005).
- Karu, A. E. & Beer, M. Pyrolytic formation of highly crystalline graphite films. *J. Appl. Phys.* **37**, 2179–2181 (1966).
- Obraztsov, A. N., Obraztsova, E. A., Tyurnina, A. V. & Zolotukhin, A. A. Chemical vapor deposition of thin graphite films of nanometer thickness. *Carbon* **45**, 2017–2021 (2007).
- Kim, K. S. *et al.* Large-scale pattern growth of graphene films for stretchable transparent electrodes. *Nature* **457**, 706–710 (2009).
- Reina, A. *et al.* Large area, few-layer graphene films on arbitrary substrates by chemical vapor deposition. *Nano Lett.* **9**, 30–35 (2009).
- Bae, S. *et al.* Roll-to-roll production of 30-inch graphene films for transparent electrodes. *Nature Nanotech.* **4**, 574–578 (2010).
- Berger, C. *et al.* Ultrathin epitaxial graphite: 2D electron gas properties and a route toward graphene-based nanoelectronics. *J. Phys. Chem. B* **108**, 19912–19916 (2004).
- Sutter, P. W., Flege, J.-I. & Sutter, E. A. Epitaxial graphene on ruthenium. *Nature Mater.* **7**, 406–411 (2008).
- Emtsev, K. V. *et al.* Towards wafer-size graphene layers by atmospheric pressure graphitization of silicon carbide. *Nature Mater.* **8**, 203–207 (2009).
- Li, X., Wang, X., Zhang, L., Lee, S. & Dai, H. Chemically derived, ultrasmooth graphene nanoribbon semiconductors. *Science* **319**, 1229–1232 (2008).
- Hernandez, Y. *et al.* High-yield production of graphene by liquid-phase exfoliation of graphite. *Nature Nanotech.* **3**, 563–568 (2008).
- Lotya, M. *et al.* Liquid phase production of graphene by exfoliation of graphite in surfactant/water solutions. *J. Am. Chem. Soc.* **131**, 3611–3620 (2009).
- Valles, C. *et al.* Solutions of negatively charged graphene sheets and ribbons. *J. Am. Chem. Soc.* **130**, 15802–15804 (2008).
- Stankovich, S. *et al.* Graphene-based composite materials. *Nature* **442**, 282–286 (2006).
- Green, A. & Hersam, M. C. Solution phase production of graphene with controlled thickness via density differentiation. *Nano Lett.* **9**, 4031–4036 (2009).
- Li, X. *et al.* Highly conducting graphene sheets and Langmuir–Blodgett films. *Nature Nanotech.* **3**, 538–542 (2008).
- Hummers, W. S. & Offeman, R. E. Preparation of graphite oxide. *J. Am. Chem. Soc.* **80**, 1339–1339 (1958).
- Brodie, B. C. Sur le poids atomique du graphite. *Ann. Chim. Phys.* **59**, 466–472 (1860).
- Mattevi, C. *et al.* Evolution of electrical, chemical, and structural properties of transparent and conducting chemically derived graphene thin films. *Adv. Funct. Mater.* **19**, 2577–2583 (2009).
- Cai, W. *et al.* Synthesis and solid-state NMR structural characterization of <sup>13</sup>C-labeled graphite oxide. *Science* **321**, 1815–1817 (2008).
- Eda, G., Fanchini, G. & Chhowalla, M. Large-area ultrathin films of reduced graphene oxide as a transparent and flexible electronic material. *Nature Nanotech.* **3**, 270–274 (2008).
- Oshima, C. & Nagashima, A. Ultra-thin epitaxial films of graphite and hexagonal boron nitride on solid surfaces. *J. Phys. Condens. Mat.* **9**, 1–20 (1997).
- Wang, J. *et al.* Synthesis of carbon nanosheets by inductively coupled radio-frequency plasma enhanced chemical vapor deposition. *Carbon* **42**, 2867–2872 (2004).
- Ferrari, A. C. *et al.* Raman spectrum of graphene and graphene layers. *Phys. Rev. Lett.* **97**, 187401 (2006).
- Acheson, E. G. Production of artificial crystalline carbonaceous materials; article of carborundum and process of the manufacture thereof carborundum. US patent 615,648 (1896).

59. Badami, D. V. Graphitization of  $\alpha$ -silicon carbide. *Nature* **193**, 569–570 (1962).
60. Isett, L. C. & Blakely, J. M. Segregation isosteres for carbon at the (100) surface of nickel. *Surf. Sci.* **58**, 397–414 (1976).
61. Gamo, Y., Nagashima, A., Wakabayashi, M., Terai, M. & Oshima, C. Atomic structure of monolayer graphite formed on Ni(111). *Surf. Sci.* **374**, 61–64 (1997).
62. Rosei, R. *et al.* Structure of graphitic carbon on Ni(111): A surface extended-energy-loss fine-structure study. *Phys. Rev. B* **28**, 1161–1164 (1983).
63. Riedl, C. *et al.* Quasi-free-standing epitaxial graphene on SiC obtained by hydrogen intercalation. *Phys. Rev. Lett.* **103**, 246804 (2009).
64. Choucair, M., Thordarson, P. & Stride, J. A. Gram-scale production of graphene based on solvothermal synthesis and sonication. *Nature Nanotech.* **4**, 30–33 (2009).
65. Wang, X. *et al.* Transparent carbon films as electrodes in organic solar cells. *Angew. Chem.* **47**, 2990–2992 (2008).
66. Wu, J., Pisula, W. & Mullen, K. Graphenes as potential material for electronics. *Chem. Rev.* **107**, 718–747 (2007).
67. Reina, A. *et al.* Transferring and identification of single- and few-layer graphene on arbitrary substrates. *J. Phys. Chem. C* **112**, 17741–17744 (2008).
68. Vijayaraghavan, A. *et al.* Dielectrophoretic assembly of high-density arrays of individual graphene devices for rapid screening. *ACS Nano* **3**, 1729–1734 (2009).
69. Beecher, P. *et al.* Ink-jet printing of carbon nanotube thin film transistors. *J. Appl. Phys.* **102**, 043710 (2007).
70. Hamberg, I. & Granqvist, C. G. Evaporated Sn-doped  $\text{In}_2\text{O}_3$  films: basic optical properties and applications to energy-efficient windows. *J. Appl. Phys.* **60**, R123–R160 (1986).
71. Holland, L. & Siddall, G. The properties of some reactively sputtered metal oxide films. *Vacuum* **3**, 375–391 (1953).
72. Minami, T. Transparent conducting oxide semiconductors for transparent electrodes. *Semicond. Sci. Technol.* **20**, S35–S44 (2005).
73. Granqvist, C. G. Transparent conductors as solar energy materials: a panoramic review. *Sol. Energy Mater. Sol. Cells* **91**, 1529–1598 (2007).
74. Sheraw, C. D. *et al.* Organic thin-film transistor-driven polymer dispersed liquid crystal displays on flexible polymeric substrates. *Appl. Phys. Lett.* **80**, 1088–1090 (2002).
75. Lee, J. Y., Connor, S. T., Cui, Y. & Peumans, P. Solution-processed metal nanowire mesh transparent electrodes. *Nano Lett.* **8**, 689–692 (2008).
76. De, S. *et al.* Silver nanowire networks as flexible, transparent, conducting films: extremely high dc to optical conductivity ratios. *ACS Nano* **3**, 1767–1774 (2009).
77. Geng, H. Z. *et al.* Effect of acid treatment on carbon nanotube-based flexible transparent conducting films. *J. Am. Chem. Soc.* **129**, 7758–7759 (2007).
78. Wu, Z. *et al.* Transparent, conductive carbon nanotube films. *Science* **305**, 1273–1276 (2004).
79. De, S. & Coleman, J. N. Are there fundamental limitations on the sheet resistance and transmittance of thin graphene films? *ACS Nano* **4**, 2713–2720 (2010).
80. Casiraghi, C., Pisana, S., Novoselov, K. S., Geim, A. K. & Ferrari, A. C. Raman fingerprint of charged impurities in graphene. *Appl. Phys. Lett.* **91**, 233108 (2007).
81. Sahu, D. R., Lin, S. Y. & Huang, J. L. ZnO/Ag/ZnO multilayer films for the application of a very low resistance transparent electrode. *Appl. Surf. Sci.* **252**, 7509–7514 (2006).
82. Gilje, S., Han, S., Wang, M., Wang, K. L. & Kaner, R. B. A chemical route to graphene for device applications. *Nano Lett.* **7**, 3394–3398 (2007).
83. Wang, X., Zhi, L. & Mullen, K. Transparent, conductive graphene electrodes for dye-sensitized solar cells. *Nano Lett.* **8**, 323–327 (2007).
84. Becerril, H. A. *et al.* Evaluation of solution-processed reduced graphene oxide films as transparent conductors. *ACS Nano* **2**, 463–470 (2008).
85. Wu, J. *et al.* Organic light-emitting diodes on solution-processed graphene transparent electrodes. *ACS Nano* **4**, 43–48 (2009).
86. Biswas, S. & Drzal, L. T. A novel approach to create a highly ordered monolayer film of graphene nanosheets at the liquid–liquid interface. *Nano Lett.* **9**, 167–172 (2008).
87. Tung, V. C. *et al.* Low-temperature solution processing of graphene-carbon nanotube hybrid materials for high-performance transparent conductors. *Nano Lett.* **9**, 1949–1955 (2009).
88. Blake, P. *et al.* Graphene-based liquid crystal device. *Nano Lett.* **8**, 1704–1708 (2008).
89. Matyba, P. *et al.* Graphene and mobile ions: the key to all-plastic, solution-processed light-emitting devices. *ACS Nano* **4**, 637–642 (2010).
90. Liu, Z. *et al.* Organic photovoltaic devices based on a novel acceptor material: graphene. *Adv. Mater.* **20**, 3924–3930 (2008).
91. Chapin, D. M., Fuller, C. S. & Pearson, G. L. A new silicon p-n junction photocell for converting solar radiation into electrical power. *J. Appl. Phys.* **25**, 676–677 (1954).
92. Green, M. A., Emery, K., Bücher, K., King, D. L. & Igari, S. Solar cell efficiency tables. *Prog. Photovolt. Res. Appl.* **7**, 321–326 (1999).
93. Hoppe, H. & Sariciftci, N. S. Organic solar cells: an overview. *MRS Bull.* **19**, 1924–1945 (2004).
94. Krebs, F. C. All solution roll-to-roll processed polymer solar cells free from indium-tin-oxide and vacuum coating steps. *Org. Electron.* **10**, 761–768 (2009).
95. O'Regan, B. & Gratzel, M. A low-cost, high-efficiency solar cell based on dye-sensitized colloidal  $\text{TiO}_2$  films. *Nature* **353**, 737–740 (1991).
96. Wu, J. *et al.* Organic solar cells with solution-processed graphene transparent electrodes. *Appl. Phys. Lett.* **92**, 263302 (2008).
97. De Arco, L. G. *et al.* Continuous, highly flexible, and transparent graphene films by chemical vapor deposition for organic photovoltaics. *ACS Nano* **4**, 2865–2873 (2010).
98. Yong, V. & Tour, J. M. Theoretical efficiency of nanostructured graphene-based photovoltaics. *Small* **6**, 313–318 (2009).
99. Yang, N., Zhai, J., Wang, D., Chen, Y. & Jiang, L. Two-dimensional graphene bridges enhanced photoinduced charge transport in dye-sensitized solar cells. *ACS Nano* **4**, 887–894 (2010).
100. Hong, W., Xu, Y., Lu, G., Li, C. & Shi, G. Transparent graphene/PEDOT-PSS composite films as counter electrodes of dye sensitized solar cells. *Electrochem. Commun.* **10**, 1555–1558 (2008).
101. Burroughes, J. H. *et al.* Light-emitting diodes based on conjugated polymers. *Nature* **347**, 539–541 (1990).
102. Pei, Q. & Heeger, A. J. Operating mechanism of light-emitting electrochemical cells. *Nature Mater.* **7**, 167 (2008).
103. Saleh, B. E. A. & Teich, M. C. *Fundamentals of Photonics* Ch. 18, 784–803 (Wiley, 2007).
104. Dawlaty, J. M. *et al.* Measurement of the optical absorption spectra of epitaxial graphene from terahertz to visible. *Appl. Phys. Lett.* **93**, 131905 (2008).
105. Wright, A. R., Cao, J. C. & Zhang, C. Enhanced optical conductivity of bilayer graphene nanoribbons in the terahertz regime. *Phys. Rev. Lett.* **103**, 207401 (2009).
106. Vasko, F. T. & Ryzhii, V. Photoconductivity of intrinsic graphene. *Phys. Rev. B* **77**, 195433 (2008).
107. Park, J., Ahn, Y. H. & Ruiz-Vargas, C. Imaging of photocurrent generation and collection in single-layer graphene. *Nano Lett.* **9**, 1742–1746 (2009).
108. Xia, F. N. *et al.* Photocurrent imaging and efficient photon detection in a graphene transistor. *Nano Lett.* **9**, 1039–1044 (2009).
109. Xia, F., Mueller, T., Lin, Y.-M., Valdes-Garcia, A. & Avouris, P. Ultrafast graphene photodetector. *Nature Nanotech.* **4**, 839–843 (2009).
110. Mueller, T., Xia, F. & Avouris, P. Graphene photodetectors for high-speed optical communications. *Nature Photon.* **4**, 297–301 (2010).
111. Kang, Y. M. *et al.* Monolithic germanium/silicon avalanche photodiodes with 340 GHz gain-bandwidth product. *Nature Photon.* **3**, 59–63 (2009).
112. Xu, X. D., Gabor, N. M., Alden, J. S., van der Zande, A. M. & McEuen, P. L. Photo-thermoelectric effect at a graphene interface junction. *Nano Lett.* **10**, 562 (2010).
113. Pickering, J. A. Touch-sensitive screens: the technologies and their applications. *Int. J. Man. Mach. Stud.* **25**, 249–269 (1986).
114. Craighead, H. G., Cheng, J. & Hackwood, S. New display based on electrically induced index-matching in an inhomogeneous medium. *Appl. Phys. Lett.* **40**, 22–24 (1982).
115. Keller, U. Recent developments in compact ultrafast lasers. *Nature* **424**, 831–838 (2003).
116. Wang, F. *et al.* Wideband-tunable, nanotube mode-locked, fibre laser. *Nature Nanotech.* **3**, 738–742 (2008).
117. Sun, D. *et al.* Ultrafast relaxation of excited Dirac fermions in epitaxial graphene using optical differential transmission spectroscopy. *Phys. Rev. Lett.* **101**, 157402 (2008).
118. Sun, Z. *et al.* Wideband tunable, graphene-mode locked, ultrafast laser. Preprint at <http://arxiv.org/abs/1003.4714> (2010).
119. Bao, Q. *et al.* Atomic-layer graphene as a saturable absorber for ultrafast pulsed lasers. *Adv. Funct. Mater.* **19**, 3077–3083 (2010).
120. Zhang, H., Bao, Q. L., Tang, D. Y., Zhao, L. M. & Loh, K. Large energy soliton erbium-doped fiber laser with a graphene-polymer composite mode locker. *Appl. Phys. Lett.* **95**, 141103 (2009).
121. Zhang, H., Tang, D. Y., Zhao, L. M., Bao, Q. L. & Loh, K. P. Large energy mode locking of an erbium-doped fiber laser with atomic layer graphene. *Opt. Express* **17**, 17630–17635 (2009).
122. Zhang, H. *et al.* Graphene mode locked, wavelength-tunable, dissipative soliton fiber laser. *Appl. Phys. Lett.* **96**, 111112 (2010).
123. Song, Y. W., Jang, S. Y., Han, W. S. & Bae, M. K. Graphene mode-lockers for fiber lasers functioned with evanescent field interaction. *Appl. Phys. Lett.* **96**, 051122 (2010).
124. Tan, W. D. *et al.* Mode locking of ceramic Nd:yttrium aluminum garnet with graphene as a saturable absorber. *Appl. Phys. Lett.* **96**, 031106 (2010).
125. Scardaci, V. *et al.* Carbon nanotube polycarbonate composites for ultrafast lasers. *Adv. Mater.* **20**, 4040–4043 (2008).



126. Sun, Z. *et al.* A compact, high power, ultrafast laser mode-locked by carbon nanotubes. *Appl. Phys. Lett.* **95**, 253102 (2009).
127. Bass, M., Li, G. & Stryland, E. V. *Handbook of Optics IV* (McGraw-Hill, 2001).
128. Wang, J., Hernandez, Y., Lotya, M., Coleman, J. N. & Blau, W. J. Broadband nonlinear optical response of graphene dispersions. *Adv. Mater.* **21**, 2430–2435 (2009).
129. Tutt, L. W. & Kost, A. Optical limiting performance of  $C_{60}$  and  $C_{70}$  solutions. *Nature* **356**, 225–226 (1992).
130. Wang, J., Chen, Y. & Blau, W. J. Carbon nanotubes and nanotube composites for nonlinear optical devices. *J. Mater. Chem.* **19**, 7425–7443 (2009).
131. Xu, Y. *et al.* A graphene hybrid material covalently functionalized with porphyrin: synthesis and optical limiting property. *Adv. Mater.* **21**, 1275–1279 (2009).
132. Mikhailov, S. A. Non-linear electromagnetic response of graphene. *Europhys. Lett.* **79**, 27002 (2007).
133. Dean, J. J. & van Driel, H. M. Second harmonic generation from graphene and graphitic films. *Appl. Phys. Lett.* **95**, 261910 (2009).
134. Hendry, E., Hale, P. J., Moger, J. J., Savchenko, A. K. & Mikhailov, S. A. Strong nonlinear optical response of graphene flakes measured by four-wave mixing. Preprint at <<http://arxiv.org/abs/0912.5321v1>> (2009).
135. Zhang, X.-C. & Xu, J. *Introduction to THz Wave Photonics* (Springer, 2010).
136. Rana, F. Graphene terahertz plasmon oscillators. *IEEE Trans. Nanotechnol.* **7**, 91–99 (2008).
137. Sun, D. *et al.* Coherent control of ballistic photocurrents in multilayer epitaxial graphene using quantum interference. *Nano Lett.* **10**, 1293–1296 (2010).
138. Otsuji, T. *et al.* Observation of amplified stimulated terahertz emission from optically pumped epitaxial graphene heterostructures. Preprint at <<http://arxiv.org/abs/1001.5075v1>> (2010).

### Acknowledgements

We thank S. A. Awan, D. M. Basko, E. Lidorikis, A. Hartschuh, J. Coleman, A. Dyadyusha, D. P. Chu, T. Etchermeyer, T. Kulmala, A. Lombardo, D. Popa, G. Privitera, F. Torrisi, O. Trushkevych, F. Wang, T. Seyller, B. H. Hong, K. S. Novoselov and A. K. Geim for discussions. We acknowledge funding from EPSRC grants EP/G042357/1 and EP/G030480/1, ERC grant NANOPOTS, a Royal Society Brian Mercer Award for Innovation, the Cambridge Integrated Knowledge Centre in Advanced Manufacturing Technology for Photonics and Electronics, and Cambridge Nokia Research Centre. F.B. acknowledges funding from a Newton International Fellowship and T.H. from King's College, Cambridge. A.C.F. is a Royal Society Wolfson Research Merit Award holder.

### Additional information

The authors declare no competing financial interests.